Fine-regolith production on asteroids controlled by rock porosity

S. Cambioni[1,2], M. Delbo[3], G. Poggiali[4], C. Avdellidou[3], A.J. Ryan[1], J.D.P. Deshapriya[5], E. Asphaug[1], R.-L. Ballouz[1], M.A. Barucci[5], C.A. Bennett[1], W.F. Bottke[6], J.R. Brucato[4], K.N. Burke[1], E. Cloutis[7], D.N. DellaGiustina[1], J.P. Emery[8], B. Rozitis[9], K.J. Walsh[6], and D.S. Lauretta[1]

(1) Lunar and Planetary Laboratory, University of Arizona, Tucson, AZ, USA; (2) Division of Geological and Planetary Sciences, California Institute of Technology, Pasadena, CA, USA; (3) Université Côte d'Azur, Observatoire de la Côte d'Azur, CNRS, Laboratoire Lagrange, Nice, France; (4) INAF – Osservatorio Astrofisico di Arcetri, Florence, Italy; (5) LESIA, Observatoire de Paris, Université PSL, CNRS, Sorbonne Université, Univ. Paris Diderot, Sorbonne Paris Cité, Meudon, France; (6) Southwest Research Institute, Boulder, CO, USA; (7) Department of Geography, University of Winnipeg, Winnipeg, MB, R3B 2E9, Manitoba, Canada; (8) Department of Astronomy and Planetary Science, Northern Arizona University, Flagstaff, AZ, USA; (9) School of Physical Sciences, The Open University, Milton Keynes, UK.

Spacecraft missions observed regolith blankets consisting of unconsolidated sub-centimetre particles on stony asteroids[1–3]. Telescopic data suggested regolith blankets to be present also on carbonaceous asteroids, including (101955) Bennu[4] and (162173) Ryugu[5]. However, despite observations of processes capable of comminuting boulders into unconsolidated materials, such as meteoroid bombardment[6,7] and thermal cracking[8], Bennu and Ryugu lack extensive areas covered in sub-centimetre particles[9,7]. Here we report an inverse

correlation between the local abundance of sub-centimetre particles and the porosity of rocks on Bennu. We interpret this finding to mean that accumulation of unconsolidated sub-centimetre particles is frustrated where the rocks are highly porous, which appears to be most of the surface[10]: these rocks are compressed rather than fragmented by meteoroid impacts, consistent with laboratory experiments[11,12], and thermal cracking proceeds more slowly than in denser rocks. We infer that regolith blankets are uncommon on carbonaceous asteroids, which are the most numerous of all asteroid types[13]. By contrast, these terrains should be common on stony asteroids, which have less porous rocks and are the second-most populous group by composition[13]. The higher porosity of carbonaceous asteroid materials may have aided in their compaction and cementation to form breccias, which dominate the carbonaceous chondrite meteorites[14].

Between April and June 2019, the Origins, Spectral Interpretation, Resource Identification, and Security-Regolith Explorer (OSIRIS-REx) Thermal Emission Spectrometer[15] (OTES) measured thermal infrared emission spectra from Bennu's surface at different local times of day. These spectra are a function of surface temperatures, which vary throughout the day and night differently depending on surface roughness and thermal inertia. Roughness (θ) is due to surface irregularities that are not resolved in global topography but still affect temperatures due to shadows and self-heating[16]. Thermal inertia (Γ) measures materials' resistance to temperature change; it is determined by thermal conductivity κ, heat capacity c_P, and bulk density ρ ($\Gamma=[\kappa c_P \rho]^{1/2}$), and allows distinguishing different geological units, such as fine regolith from rocks.

Here fine regolith means unconsolidated particles of size smaller than the e-folding depth of the diurnal thermal wave (l_s, a few centimetres on Bennu[10]), while rocks are defined as every competent surface material of size $D_R > l_s$. The thermal inertia of fine regolith (Γ_P) is lower than that of rocks of same composition (Γ_R) because radiative thermal conduction between particles is less efficient than phononic heat transfer within an individual particle or rock[16]. Thus, fine regolith is hotter than rocks during the day, and vice versa during the night. Both fine regolith and rocks contribute to the infrared emission proportionally to their surface abundances α and $(1-\alpha)$, respectively[17].

To distinguish fine regolith from rocks on Bennu, we use a machine learning method[17] that explores all possible combinations of the spectral signals of fine regolith and rocks as a function of their surface abundance, roughness and respective thermal inertia until the OTES daytime and night-time observations are simultaneously fitted (Methods). We use our method to derive Γ_P, Γ_R, and α in 122 quasi-randomly–distributed OTES footprints (spots) of ~40 m in diameter (Supplementary Table 1; Extended Data Figure 1). These spots include the two best-observed areas on Bennu: the designated backup and primary sampling sites of OSIRIS-REx, respectively called Osprey and Nightingale.

We find that α varies between a few and several tens of percent (Figure 1) and there is less fine regolith at Osprey than at Nightingale, consistent with the surface abundance of unresolved materials seen in PolyCam images (Extended Data Figure 2). The values of α are also consistent with the surface abundance of unresolved materials in PolyCam images at coarser spatial resolution (Methods; Extended Data Figure 3). The measured Γ_R encompasses a continuum of

values between ~250 $Jm^{-2}K^{-1}s^{-0.5}$, close to that derived[18,19] for Ryugu's boulders, and >1,000 $Jm^{-2}K^{-1}s^{-0.5}$, close to that of CM2 carbonaceous chondrites[20] of composition analogous to the one spectroscopically inferred for Bennu[21]. For $\alpha \approx 0$, Γ_R is within the range of thermal inertia values derived by a previous study[10], which assumed that the surface in the OTES spot is composed of a single geological unit.

We observe a direct correlation between of Γ_R and α (Figure 1), with Spearman correlation coefficient $R=0.56\pm0.06$ and a probability of non-correlation $p<4\times10^{-3}$ (Methods; Extended Data Figure 4). The correlation is robust ($R=0.54\pm0.07$; $p<0.05$) when we reject spots where the thermophysical model may confuse very low-Γ_R boulders as fine-regolith–covered areas (Methods; Figure 1). The correlation is also robust against the choice of a model parameter that represents the fine-regolith macroporosity (Methods; Extended Data Figure 5). Additionally, we demonstrate that the correlation is not an artefact of thermophysical modelling (Methods; Extended Data Figure 6). Finally, we do not see an inverse correlation between α and the size of the largest boulders in the OTES spots (Methods; Extended Data Figure 7), thus ruling out that the Γ_R-α correlation is due to boulders' sizes (large boulders may have lower Γ_R than smaller ones[10]).

Because fine regolith is more abundant where rocks have higher Γ_R (Figure 1), and Γ_R is a monotonically decreasing[19] function of rock porosity (Methods), we deduce that the surface abundance of fine regolith is lower where the nearby rocks are more porous (Figure 1).

We argue that the correlation of Figure 1 can be explained by the dependence of regolith-forming processes, i.e., collisional and thermal fragmentation of rocks, on rock porosity.

Collisional fragmentation is driven by meteoroid impacts, craters from which were observed[6] on $D_R >> l_s$ rocks. Craters on rough-textured rocks were measured, by means of the OSIRIS-REx Laser Altimeter, to have a higher depth-to-diameter ratio than those on smoother rocks[6]. Because crater depth-to-diameter ratio typically increases with increasing target porosity[11,22], we deduce that Bennu hosts rocks of different porosities, consistent with Figure 1 and ref. 10, but independently of OTES data. Impact experiments show that: (i) a lower-porosity rock requires a lower energy per unit mass to be broken than a higher-porosity rock, because in the latter impact energy is spent on pore-space collapse[11] and compaction[12] during initial crater formation; (ii) crater ejecta's mass, which could partially contribute to fine regolith, decreases with increasing target porosity[11]; and (iii) craters formed on low-porosity ($\Phi \approx 25\%$) rock simulants of Bennu's composition have spalls[23], which increase fragment production. Conversely, spalling was rarely observed around craters on Bennu's rocks[6]. We deduce that collisional fragmentation increases with decreasing rock porosity and is frustrated on Bennu's rocks, which typically have $\Phi > 25\%$ (Figure 2).

Asteroids' rocks can develop fatigue fractures to release mechanical stresses generated by diurnal temperature cycling[24]. It is postulated that these fractures grow until breaking the host rocks, thereby producing regolith[24]. Exfoliation fractures with sizes between a few centimetres and few metres were observed[8] on Bennu, consistent with the aforementioned process. To investigate regolith formation by thermal fatigue, we model (Methods) the time to break two rocks on Bennu

that have porosity Φ=20% and Φ=40%. We find that the break-up time is shorter for the rock with Φ=20% than for that with Φ=40% (Extended Data Figure 8), suggesting that fine regolith is more likely to be produced from the former. This is consistent with the correlation of Figure 1.

We infer that low-porosity rocks produce more fine regolith than high-porosity rocks by means of both meteoroid impacts and thermal cracking (Figure 3). This explains the lack of extensive fine-regolith–covered areas on Bennu[9], where most rocks are highly porous (ref. 10; Figure 2).

We argue that the frustration of fine-regolith build-up in the presence of high-porosity rocks could be a general phenomenon on asteroids.

Analysis of thermal images acquired by JAXA's Hayabusa2 mission[18,25] indicated that Ryugu's surface globally has $\Gamma \approx 225 \pm 45$ $Jm^{-2}K^{-1}s^{-0.5}$, some D_R>50 m boulders have $\Gamma_R \approx 115$–160 $Jm^{-2}K^{-1}s^{-0.5}$, and a few small boulders have $\Gamma_R \approx 600$–$1{,}000$ $Jm^{-2}K^{-1}s^{-0.5}$, suggesting that most rocks on Ryugu have porosities similar to Bennu's ($\Phi \approx 40$–50%, Figure 2; Methods). For $\Phi \approx 40$–50%, the correlation of Figure 1 indicates that Ryugu, like Bennu, should have less fine regolith on the surface than asteroids with lower-porosity rocks.

Conversely, disk-integrated infrared measurements of the stony asteroid (25143) Itokawa revealed[17] that its rocks have $\Gamma_R \approx 900$ $Jm^{-2}K^{-1}s^{-0.5}$, corresponding to $\Phi = 20 \pm 4$% (Methods), which is lower than most rocks on Bennu and Ryugu (Figure 2). Hence, the correlation of Figure 1 implies that Itokawa's most common rocks produce more fine regolith than Bennu's and Ryugu's. Spacecraft images show that Itokawa's geopotential lows are smooth terrains covered in

centimetre-sized regolith[2], whereas Bennu's and Ryugu's are not[9,7]. Itokawa's smooth terrains may have formed via global particle-size sorting induced by surface mass motion[2]. Signatures of mass motion were also observed on Bennu[26] and Ryugu[7], but smooth fine-regolith–covered terrains are lacking[9,7], suggesting that Bennu's and Ryugu's surface abundances of fine regolith may be globally lower than Itokawa's. This is consistent with our analysis.

On small asteroids, fine regolith could be emplaced far from the source rock via electrostatic lofting[27], ejection during thermal exfoliation[8], and/or meteoroid impacts[22]. However, the robustness of the Γ_R-α correlation rules out an isotropically fine-regolith redistribution from each local source on Bennu. Further, (i) electrostatic lofting is inefficient at mobilizing centimetre-sized particles[27]; (ii) exfoliation is only one aspect of thermal cracking, the other being rock breakup by through-going fracturing without fragment ejection; (iii) the current understanding[22] is that little mass should be retained by small asteroids from crater ejecta produced by impacts on low-porosity rocks. However, rocks broken in tightly-clustered pieces were observed on Bennu (Extended Data Figure 9; refs. 8, 9, and 28), suggesting that regolith is produced by in-situ fragmentation of large rocks exposed on the surface, similar to what has been observed on the Moon[29]. Finally, Itokawa may lose more crater ejecta to space than Bennu and Ryugu because average ejection velocities decrease with increasing target porosity[22]. Despite this, smooth terrains were only observed on Itokawa[2,7,9], suggesting that its fine-regolith losses are compensated by a higher production than Bennu's and Ryugu's.

The wide range of rock porosities measured on Bennu and Ryugu likely originated on their parent bodies[25]. We postulate that high-porosity rocks subjected to impacts can be compacted

without target disruption[30]. Crushing in high-porosity materials can enhance shear strain and cause associated frictional heating[31]; this may have assisted lithification of the chondrite precursors into the lower-porosity carbonaceous breccias that dominate the CM and CI meteorite collection[14] and were also observed on Bennu[28] and Ryugu[7].

1. Veverka, J. et al. The landing of the NEAR-Shoemaker spacecraft on asteroid 433 Eros. *Nature* **413**, 390–393 (2001).
2. Miyamoto, H. et al. Regolith migration and sorting on asteroid Itokawa. *Science* **316**, 1011–1014 (2007).
3. Huang, J. et al. The Ginger-shaped Asteroid 4179 Toutatis: New observations from a Successful Flyby of Chang'e-2. *Scientific reports* **3**, 3411 (2013).
4. Emery, J. et al. Thermal infrared observations and thermophysical characterization of OSIRIS-REx target asteroid (101955) Bennu. *Icarus* **234**, 17–35 (2014).
5. Müller, T. et al. Hayabusa-2 mission target asteroid 162173 Ryugu (1999 JU3): Searching for the object's spin-axis orientation. *Astronomy & Astrophysics* **599**, A103 (2017).
6. Ballouz, R.-L. et al. Bennu's near-Earth lifetime of 1.75 million years inferred from craters on its boulders. *Nature* **587**, 205–209 (2020).
7. Sugita, S. et al. The geomorphology, color, and thermal properties of Ryugu: Implications for parent-body processes. *Science* **364**, 6437 (2019).
8. Molaro, J. L. et al. Thermal fatigue as a driving mechanism for activity on asteroid Bennu. *Journal of Geophysical Research: Planets* **125**, e2019JE006325 (2020).
9. Lauretta, D. et al. The unexpected surface of asteroid (101955) Bennu. *Nature* **568**, 55–60 (2019).

10. Rozitis, B. et al. Asteroid (101955) Bennu's weak boulders and thermally anomalous equator. *Science Advances* **6**, 41 (2020).
11. Flynn, G. J. et al. Hypervelocity cratering and disruption of porous pumice targets: Implications for crater production, catastrophic disruption, and momentum transfer on porous asteroids. *Planetary and Space Science* **107**, 64–76 (2015).
12. Housen, K. R., Sweet, W. J. & Holsapple, K. A. Impacts into porous asteroids. *Icarus* **300**, 72–96 (2018).
13. DeMeo, F., Alexander, C., Walsh, K., Chapman, C. & Binzel, R. The compositional structure of the asteroid belt. In *Asteroids* **IV**, 13–41 (2015).
14. Bischoff, A., Scott, E. R. D., Metzler, K. & Goodrich, C. A. Nature and Origins of Meteoritic Breccias. In *Meteorites and the Early Solar System* **II**, 679 (2006).
15. Christensen, P. R. et al. The OSIRIS-REx thermal emission spectrometer (OTES) instrument. *Space Science Reviews* **214**, 87 (2018).
16. Delbo, M., Mueller, M., Emery, J. P., Rozitis, B. & Capria, M. T. Asteroid Thermophysical Modeling. In *Asteroids* **IV**, 107–128 (2015).
17. Cambioni, S., Delbo, M., Ryan, A. J., Furfaro, R. & Asphaug, E. Constraining the thermal properties of planetary surfaces using machine learning: Application to airless bodies. *Icarus* **325**, 16–30 (2019).
18. Shimaki, Y. et al. Thermophysical properties of the surface of asteroid 162173 Ryugu: Infrared observations and thermal inertia mapping. *Icarus* **348**, 113835 (2020).
19. Grott, M. et al. Low thermal conductivity boulder with high porosity identified on C-type asteroid (162173) Ryugu. *Nature Astronomy* **3**, 971–976 (2019).

20. Opeil, C. P., Britt, D. T., Macke, R. J. & Consolmagno, G. J. The surprising thermal properties of CM carbonaceous chondrites. *Meteoritics and Planetary Science* **55**, E1–E20 (2020).
21. Hamilton, V. et al. Evidence for widespread hydrated minerals on asteroid (101955) Bennu. *Nature Astronomy* **3**, 332–340 (2019).
22. Michikami, T., Moriguchi, K., Hasegawa, S. & Fujiwara, A. Ejecta velocity distribution for impact cratering experiments on porous and low strength targets. *Planetary and Space Science* **55**, 70–88 (2007).
23. Avdellidou, C. et al. Very weak carbonaceous asteroid simulants I: Mechanical properties and response to hypervelocity impacts. *Icarus* **341**, 113648 (2020).
24. Delbo, M. et al. Thermal fatigue as the origin of regolith on small asteroids. *Nature* **508**, 233–236 (2014).
25. Okada, T. et al. Highly porous nature of a primitive asteroid revealed by thermal imaging. *Nature* **579**, 518–522 (2020).
26. Jawin, E. et al. Global patterns of recent mass movement on asteroid (101955) Bennu. *Journal of Geophysical Research: Planets* **125**, e2020JE006475 (2020).
27. Hsu, H., Wang, X., Carroll, A., Hood, N. & Horanyi, M. Electrostatic removal of fine-grained regolith on sub-km asteroids. In *AAS/Division for Planetary Sciences Meeting Abstracts* **52**, 402.06 (2020).
28. Walsh, K. et al. Craters, boulders and regolith of (101955) Bennu indicative of an old and dynamic surface. *Nature Geoscience* **12**, 242–246 (2019).
29. Ruesch, O. et al. In situ fragmentation of lunar blocks and implications for impacts and solar-induced thermal stresses. *Icarus* **336**, 113431 (2020).

30. Scott, E. R. D. & Bottke, W. F. Impact histories of angrites, eucrites, and their parent bodies. *Meteoritics and Planetary Science* **46**, 1878–1887 (2011).
31. Bland, P. A. et al. Pressure-temperature evolution of primordial solar system solids during impact-induced compaction. *Nature Communications* **5**, 5451 (2014).

Fig. 1. The thermal inertia of Bennu's rocks is positively correlated with the local surface abundance of fine regolith. The data points are grey-shaded in terms of Φ estimated from Γ_R (Methods). The red points correspond to 13 areas where α could be overestimated because of the presence[10] of boulders whose Γ_R could be lower than the threshold value between fine regolith and rocks (Methods). The plotted solutions have $\chi^2_r<3$ as goodness-of-fit (Methods), which is satisfactory for these types of observations. The error bars correspond to 1 standard deviation (Supplementary Table 1; Methods) computed on ~670 samples on average.

Fig. 2. The porosity of most of Bennu's and Ryugu's rocks is much higher than Itokawa's. The porosity values of Bennu's rocks are weighted according to rock abundance ($1-\alpha$) and are binned using the Freedman-Diaconis rule. The magenta- and green-shaded areas indicate the estimated surface-averaged ranges of rock porosity on asteroids Ryugu[18,19] and Itokawa[17], respectively. About 70% of the rocks on Bennu are as porous as Ryugu's, while only ~5% of Bennu's rocks have porosity similar to Itokawa's.

Fig. 3. Fine-regolith production is frustrated in the presence of high-porosity rocks. On asteroids, rocks with higher porosity are compacted by meteoroid impacts rather than

excavated[12]. Thermal stresses in a more porous rock are weaker in magnitude than in a denser rock[8], implying that the former could be less prone to producing fine regolith than the latter.

Methods

Two-component thermophysical modelling

The global mosaic of images[32] acquired by the PolyCam imager of the OSIRIS-REx Camera Suite (OCAMS[33]) with resolution 5 cm pixel^{-1} shows that Bennu's surface is composed of a mixture of rocks and, to a lesser extent, unresolved materials[28,34]. The latter may include fine regolith with particle size $D_P<l_s=[\kappa/(c_P\rho)P/\pi]^{1/2}$, where P is the asteroid's rotation period. These observations motivate us to determine the surface abundance of fine regolith (α) with respect to the surface abundance ($1-\alpha$) of rocks with size $D_R>l_s$.

To this end, we select 122 quasi-randomly–distributed regions (OTES spots; Extended Data Figure 1) and use a machine learning two-component thermophysical model[17] to simultaneously fit infrared radiance spectra emitted from the asteroid at the local times 3:20 a.m. and 3:00 p.m. to derive the surface properties (θ, Γ_P, Γ_R, α). The 3:20 a.m. station is the coldest and farthest in time from sunrise, when the brightness temperature of smaller rocks may approach that of colder fine regolith; the 3:00 p.m. station is diametrically opposed to the 3:20 a.m. station, close to the time of peak surface temperature, and not at the crossing point between diurnal temperature curves for different Γ values, where the thermophysical solution could be degenerate (Figure 2 in ref. 10). Furthermore, the spots on the surface for the 3:00 p.m. and 3:20 a.m. stations are well aligned, which minimises mismodelling. Modelling 122 areas instead of the full surface makes the machine-learning analysis computationally feasible while still investigating a representative

sample of Bennu's surface. Among the 122 spots, 100 are randomly selected and 22 were manually added to be centred as much as possible on distinct, interesting and representative geological features such as (i) the designated sampling sites; (ii) large boulders filling the OTES spot; (iii) regions with high boulder abundance; and (iv) areas with low boulder abundance.

For each area and time of day, we use the OTES' acquisition mid-observation time and boresight to calculate the longitude and latitude of the OTES spot's centre and diameter projected on Bennu's surface. The surface is modelled using the 6-m–resolution SPC/OLA v34 shape model composed of triangular facets and derived from a combination of stereophotoclinometry and laser ranging[35]; its pole orientation[9,10] is J2000 ecliptic longitude 69.92° and latitude -83.45°. The observation geometry for each spot and time of the day (i.e., ephemerides of the OSIRIS-REx spacecraft and the asteroid) is computed using the spiceypy Python-wrapper for the SPICE Toolkit. The kernel files are directly sourced from the SPICE kernels produced by the mission. For each observation geometry, we build the local set of facets of Bennu's topographic model by drawing concentric circles (with radius ranging between 0 and that of the OTES spot and centred at the spot's centre) and by drawing radial vectors with origin in the spot's centre and length between 0 and the spot's radius. Since we limited our survey to latitudes between ±60°, each OTES spot is well-approximated by a circle with a diameter of 40 m that corresponds to the instrument footprint. All the unique facets that lie at the intersection between a circle and a radial vector belong to the local set.

For each OTES spot and for each observation time, we set up thermophysical simulations using a well-defined model[16] that uses the aforementioned observation geometry, asteroid illumination,

asteroid spin state, and local sets of facets of Bennu's shape model as input. We create lookup tables of simulations where Γ varies between 25 and 2,500 $Jm^{-2}K^{-1}s^{-0.5}$ (the upper limit corresponding to low-porosity meteorites[20]) with step 25 and θ is modelled using hemispherical craters with surface crater density (f_c) ranging between 0 and 0.99 with step 0.14 (as such, $\theta=49f_c^{1/2}$ represents roughness RMS slope[10]). We assume a fixed value of Bolometric Bond's albedo equal to 0.02 and infrared emissivity $\varepsilon=0.95$ (as previously done[10]). The shape model's rotation and daily temperature cycle are simulated for 15 Julian days until the temperature cycle converges to a stable cycle. After this, we output the simulated radiance at the epoch of the OTES observation between 6 and 50 μm, where the OTES noise equivalent spectral radiance (NESR, which represents the 1σ variation in calibrated radiance) is the lowest[15].

Next, for each OTES spot and for each observation time, we use the aforementioned look-up table of thermophysical simulations to train a neural network that generalizes the prediction of the radiance as a function of Γ and θ. The step of training the neural networks and using them in the fitting routine makes the exploration of the large, multi-dimensional parameter space of solutions computationally possible. This approach is particularly potent for the case of Bennu as both day-side and night-side data are available with a wide spectral wavelength range[15,17]. The 70% of model radiances is used for training via stochastic gradient descent and a neural network architecture with 1 hidden layer of 10 neurons, which is the optimal scheme[17]. Another 15% of the dataset is used to protect the networks against overfitting the training data. We use the last 15% of the dataset to assess the networks' performance on unseen data in terms of mean squared error between the predicted and target radiances. The networks generalise well the prediction of the model radiances at testing: the average errors are equal to 0.2% and 0.9% of the radiance

peak value for Γ=350 $Jm^{-2}K^{-1}s^{-0.5}$ and θ=43° (which are the average surface thermophysical properties of Bennu[10]) for the 3:20 a.m. and 3:00 p.m. observations, respectively; the correlation coefficient between predicted and target radiances is >0.99.

Next, we use the networks to simulate the radiance $L_{regolith}$ emitted by fine regolith of thermal inertia Γ_P and that emitted by rocks of thermal inertia Γ_R (L_{rock}), and linearly combine them to model the radiance L_{model} emitted by a mixture of fine regolith and rocks:

$$L_{model}[f_s, \theta, \Gamma_P, \Gamma_R, \alpha]=f_s\times(\alpha L_{regolith}[\Gamma_P, \theta]+(1-\alpha)L_{rock}[\Gamma_R, \theta]), \quad (1)$$

where f_s is an optional scaling factor which is adjusted during the model fit to account for small modelling errors caused by (unknown) inaccuracies in the topographic model and/or potential deficiencies of the surface roughness[10]. Γ_P can assume values between 25 $Jm^{-2}K^{-1}s^{-0.5}$ and Γ_c, and Γ_R between Γ_c and 2,500 $Jm^{-2}K^{-1}s^{-0.5}$, where Γ_c is the thermal inertia "cut-off" value of regolith whose particles have $D_P=l_s$. It is computed as follows. For each area, we postulate that fine regolith is produced by the comminution of local rocks by meteoroid impacts[36] and thermal cracking[24]. This implies that fine regolith particles inherit the thermal conductivity κ, grain density ρ_s, and porosity Φ of the rock. κ is obtained using the fit of meteorite values[37]

$$\kappa(\Phi)=\frac{\Gamma_R^2}{c_P\rho_s(1-\Phi)}=\frac{0.11(1-\Phi)}{\Phi} \quad (2)$$

where ρ_s=2920 kg m^{-3} for CM meteorites[38] and c_P is the heat capacity for the meteorite CM2 Cold Bokkeveld[20] at the OTES spot's mean diurnal temperature[10]. Although alternative relationships of thermal conductivity versus rock porosity are available[19], Eq. 2 is the model that also fits well more recent results for super-weak CM-like materials[23]. Since Γ_R is a fitted parameter, the procedure for determining Γ_c is necessarily iterative; we initialise the iteration assuming Γ_R equal to the single-component thermal inertia derived by previous studies[10]. We use

a standard[39] regolith model to calculate particulate regolith bulk thermal conductivity (κ_P) as a function of particle diameter D_P. These values are compared to respective values of $l_s=l_s(\kappa_P)$ to find the value of κ_P where $D_P=l_s$. This value of κ_P is combined with c_P and $\rho=\rho_s\times(1-\Phi)\times(1-\varphi)$ to calculate Γ_c (φ is the regolith macroporosity, that is, the volume of voids between particles). We use published[10] model parameters and assume: $\zeta=0.68+7.6\times10^{-5}D_P^{-1}$ as the ratio of the effective distance of radiative heat transfer in the voids between particles to the void geometric size[39,40], $\xi=0.12$ as the degree of reduction of the thermal conductance at the contacts between particles owing to the microscopic surface roughness[39], infrared emissivity[10] $\varepsilon=0.95$, and regolith macroporosity $\varphi=40\%$. The latter is an often-used value and represents a loose random packing of spherical particles[41]. We take into account thermal gradients within individual regolith particles using the non-isothermal correction factor[41] as in previous work[10].

For a given Γ_c and assuming θ from published[10] results, we explore all possible combinations of the free parameters $x=(f_s^{3:00\ p.m.}, f_s^{3:20\ a.m.}, \Gamma_P, \Gamma_R, \alpha)$ to identify the best-fit radiance that minimises the error function:

$$\chi^2_r=\frac{1}{\text{obs-df}}\left(\sum_{\lambda=6}^{50\ \mu m}\frac{[L_{model}^{3:00\ p.m.}(x,\lambda)-L_{OTES}^{3:00\ p.m.}(\lambda)]^2}{\sigma^2}+\sum_{\lambda=6}^{50\ \mu m}\frac{[L_{model}^{3:20\ a.m.}(x,\ \lambda)-L_{OTES}^{3:20\ a.m.}(\lambda)]^2}{\sigma^2}\right) \quad (3)$$

where L_{OTES} is the observed radiance re-sampled with step 1 μm, σ is the error measurement equal to 3 times the OTES' pre-flight[15] 772 Hz NESR, obs is the number of observations and df=5 is the number of parameters to fit. The uncertainties of the free parameters are computed as the standard deviation of the set of solutions whose $\chi^2_r<\min(\chi^2_r)+[2/(\text{obs}-\text{df})]^{1/2}$, as typically done in thermophysical modelling[42]. Upon completion of the fitting, the best-fit Γ_R is used to update the value of Γ_c, which is in turn used to re-compute the best-fit ($f_s^{3:00\ p.m.}$, $f_s^{3:20\ a.m.}$, Γ_P, Γ_R, α). This loop is repeated until $|\Gamma_R^{\,i}-\Gamma_R^{\,i-1}|<\sigma_R^{\,i-1}$, where (i) indicates the present iteration and $\sigma_R^{\,i-1}$

366 is the standard deviation of Γ_R obtained at the iteration (i−1)-th. Convergence is typically reached
367 in four iterations. Once the analysis is completed, we add a cautionary 10% relative error to the
368 uncertainties because previous studies[10] found that the thermophysical solution obtained by
369 fitting the 3:00 p.m. and 3:20 a.m. data is within 10% of the value obtained by including
370 additional OTES data acquired at other times of the day.
371
372 Finally, we reject 25 spots where the best-fit solutions have $\chi^2_r>10$ and/or for which no
373 convergence is found for $\Gamma_R \leq 2490$ $Jm^{-2}K^{-1}s^{-0.5}$. We carry the analysis and tests reported below
374 on the remaining 97 spots (Supplementary Table 1).
375
376 **Tests of the robustness of the results**
377 We test whether the measured α-values are consistent with the surface abundance of unresolved
378 materials seen in PolyCam[33] images. We do this test for the spots 609505286:610098718 and
379 609504794:610100730 centred at Osprey and at Nightingale, for which Burke et al. (ref. 43)
380 performed rock mapping down to $D_P=2$ cm$\lesssim l_s$ (results are in Extended Data Figure 2). We note
381 that the OTES spots have areas at least 38 and 20 times larger than those within which rocks
382 were visually mapped at Osprey and Nightingale, respectively.
383
384 We also test that the value of α is always smaller or equal than the surface area of unresolved
385 materials that we can visually see, at coarser spatial resolution than at Osprey and Nightingale,
386 within the entire OTES spot. We choose the spots 609493058:610103962 and
387 609487186:610098206 where we perform rock mapping as similarly done in ref. 43 on PolyCam
388 images at a spatial resolution of 5 cm $pixel^{-1}$ (thus, $>l_s$). The area of each rock is computed as

389 that of a circle with diameter equal to the rock's longest dimension. One minus the sum of rocks'
390 areas divided by the area of the OTES spot is provided as % of unresolved material in Extended
391 Data Figure 3, along with the value of α. We also check that the size distributions of the mapped
392 rocks are consistent with that globally mapped on Bennu[34], meaning that the two sites are
393 representative of average Bennu.
394
395 We use the two-sided Spearman test to reject the null hypothesis that a random distribution of
396 Γ_R- and α-values could produce the observed correlation of Figure 1 (Extended Data Figure 4).
397 To take into account uncertainties in the values of Γ_R and α, we perform the Spearman test
398 10,000 times, where at each trial we vary Γ_R and α within their uncertainties. We draw the
399 samples from Gaussian distributions with mean and standard deviation equal to the nominal
400 value and uncertainties of Γ_R and α.
401
402 We repeat the Spearman test after we reject 13 areas where large dark boulders fill the OTES
403 spot (red data points in Figure 1). Bennu's dark boulders tend to have low Γ_R values[10,34], although
404 the lower limit of Γ_R is unknown because only one boulder was spatially resolved by the OTES
405 instrument[10]. If the boulders' $\Gamma_R<\Gamma_c$, their surface abundance would erroneously contribute to the
406 surface abundance of fine regolith α instead of being counted as rocks, with the caveat that fine
407 regolith could be present on top of the boulders[10].
408
409 We investigate whether the Γ_R-α correlation is sensitive to the assumed value of regolith
410 macroporosity φ (Extended Data Figure 5). We repeat the thermophysical modelling of all OTES
411 spots for a low-end value of φ=15%, which is an estimate for the whole asteroid based on a

412 boulder size-frequency distribution analysis[44], and a high-end value of φ=60%, which is a
413 compromise reduction from much higher values used in previous studies (e.g. φ=80%, ref. 45,
414 which we consider unlikely for a polydisperse size-frequency-distribution). We perform a 3σ test
415 on the solutions to identify those areas where (Γ_P, Γ_R, α) for φ=15% and φ=60% are statistically
416 distinct from those for φ=40%. This test is done considering only those spots where a converged
417 solution is found for both macroporosities: 93 spots (φ=40% versus φ=15%) and 90 spots
418 (φ=40% versus φ=60%). We repeat the Spearman test to assess the robustness of the correlation
419 against removing the areas with statistically distinct solutions from the dataset.
420
421 We investigate whether the Γ_R-α correlation may be an artefact due to the assumption of linear
422 mixing between the radiances emitted by fine regolith and rocks (Eq. 1). We simulate synthetic
423 radiances emitted from a single triangular facet with zero roughness and thermal inertia values
424 following the step function Γ(α): $\Gamma \leq \Gamma_c = 100$ $Jm^{-2}K^{-1}s^{-0.5}$ for α=100% and $100 < \Gamma < 2{,}500$
425 $Jm^{-2}K^{-1}s^{-0.5}$ for α=0%. We simulate the observation of these model radiances by OTES and fit
426 them using our thermophysical model to see whether we retrieve the modelled step function or a
427 correlation similar to that of Figure 1 is instead obtained (Extended Data Figure 6).
428
429 Finally, it has been suggested[10,34,46] that dark boulders (normal reflectance 0.034–0.049) are more
430 abundant, can reach higher diameters, and have lower thermal inertia than the bright boulders
431 (normal reflectance 0.049–0.074). These boulder properties could mimic the Γ_R-α correlation of
432 Figure 1 if α was also negatively correlated with the area of the largest boulder in the OTES spot.
433 Using the boulder database of ref. 46 we plot the α-value as a function of the size of the largest

boulder and perform the Spearman test to investigate whether these quantities are correlated (results are in Extended Data Figure 7).

Interpretation of the results

For each OTES spot, we compute the rock porosity Φ from the best-fit Γ_R by means of Eq. 2, assuming ρ_s and c_P as for the computation of Γ_c. The range of Φ-values for Ryugu in Figure 2 corresponds to that estimated[19] using Eq. 2 for the boulder observed by the MASCOT infrared radiometer, whose type is typical[25] on Ryugu. We use Eq. 2 also to compute Φ of the rocks on Itokawa from the published[17] value of Γ_R=894±122 $Jm^{-2}K^{-1}s^{-0.5}$ assuming the composition of LL chondrites, which is that of the samples returned from Itokawa[47]: ρ_s=3220 kg m^{-3} and c_P=682 $Jkg^{-1}K^{-1}$. We compute the uncertainty of Itokawa's Φ as $\sigma(\Phi)=\partial\Phi/\partial\Gamma_R\times\sigma(\Gamma_R)$, where $\sigma(\Gamma_R)$ is the uncertainty of Itokawa's Γ_R from ref. 17.

Next, we use this information to estimate the time to break a rock of diameter D_R by thermal fatigue (t_B). We use known models[24,48] to simulate a bed of polydispersed spherical rocks, whose surface is exposed to cyclic temperature variations driven by sunlight; on each rock, an initially sub-mm-sized fracture placed on the surface propagates downward in the rock (i.e., towards the centre of the asteroid), until its size, a, becomes equal to D_R, which is the condition for rock break-up. The time to fracture, t_B, can be calculated from the fracture growth rate da/dN, which is typically approximated[24] using Paris' law: $da/dN=C[\Delta K_I(a)]^n$, where N is the number of temperature cycles, C and n have values determined from experiments or analogy with asteroid simulant materials[24], and ΔK_I is the maximum variation of the stress intensity factor (K_I) for fracture opening mode. The latter is related to the stress τ experienced by the material during a

temperature cycle. $\Delta K_I \propto \tau \propto \Delta T$, which is the maximum diurnal temperature excursion[24]. Moreover, from Eq. 23 of ref. 48 we can write that $t_B/P=\Lambda'(D_R/l_s)^{1/m}$, where P is the asteroid rotation period; $m=1/(1-n)$ for $D_R/l_s \leq 1$ and $m=1/(n-1)$ for $D_R/l_s>1$. Hence:

$$\frac{t_B}{P}=N=\Lambda'' \left(\frac{D_R}{l_s}\right)^{\frac{1}{m}} (\Delta T)^{-n} \quad (4)$$

Given N cycles required to break a rock with a certain D_R/l_s, material properties, geometry and ΔT, we derive the value of Λ'' and use Eq. 4 to predict t_B for rocks of different sizes at different ΔT. First, we calculate l_s to be 6.4 and 8.6 cm for the carbonaceous and the ordinary chondrite of ref. 24 for which, at $D_R=l_s$, their Figure 1 gives $t=3.5\times10^3$ and 6.3×10^3 years, respectively, corresponding to $N=1.4\times10^6$ and $N=14\times10^6$ cycles, given their P=6 hours. We take ΔT from their Extended Data Figure 2. Next, we use Eq. 4 to derive t_B as a function of D_R for values of l_s, P and ΔT that are more appropriate for Bennu, Ryugu and Itokawa than those of ref. 24. From the latter reference we take the carbonaceous chondrite properties, but we use $\Gamma_R=500$ $Jm^{-2}K^{-1}s^{-0.5}$, which is more appropriate for the high-Φ, low-Γ_R rocks that dominate Bennu's and Ryugu's surfaces (Figure 2 and ref. 18, 19, 25, respectively). For the ordinary chondrite, we use $\Gamma_R=900$ $Jm^{-2}K^{-1}s^{-0.5}$, as the latter value was derived from astronomical observations[17] of Itokawa, and we assume that these parameters could also represent low-Φ, high-Γ_R rocks which may be present on Bennu's and Ryugu's surface, but in lower abundance than the high-Φ, low-Γ_R rocks. The rotation periods are P=4.296, 7.63, and 12.1 hours for Bennu[49], Ryugu[50], and Itokawa[51], respectively. However, since these rotation periods could have been different[49] in the past, due to the Yarkovsky–O'Keefe–Radzievskii–Paddack (YORP) effect, we consider generic low-Γ_R, high-Φ and high-Γ_R, low-Φ cases with P=4.296 and 12.1 hours for a total of four cases. For each of them we calculate their l_s-values and run a thermophysical model to determine, at 1.2 au of

heliocentric distance, the values of ΔT. Finally, using Eq. 4 we produce the Extended Data Figure 8.

Data Availability

Raw through calibrated OTES[52] and OCAMS[53] data are available via the Planetary Data System at https://sbn.psi.edu/pds/resource/orex/. The SPC/OLA v34 shape model is available via the Small Body Mapping Tool at http://sbmt.jhuapl.edu/. The IDs of the OTES observations used in this study and the best-fit solutions for the thermophysical model are in Supplementary Table 1. The boulder size, location and reflectance used to test the robustness of the results are in refs. 34 and 46.

Code Availability

The thermophysical analysis reported here uses a custom code based on the Thermophysical Model of ref. 16, available at www.oca.eu/images/LAGRANGE/pages_perso/delbo/thermops.tar.gz. The code to compute the geometry of the OTES acquisitions and boresight is available in Zenodo with the identifier 10.5281/zenodo.4781752 (ref. 54). The code to compute the values of Γ_c for the thermophysical analysis is available in Zenodo with the identifier 10.5281/zenodo.4763783 (ref. 55). The rock mapping of Extended Data Figure 3 was performed using the SAOImageDS9 software available at cfa.harvard.edu/saoimageds9. Other codes that support the findings of this study are available in Zenodo with the identifier 10.5281/zenodo.4771035 (ref. 56).

32. Bennett, C. et al. A high-resolution global basemap of (101955) Bennu. *Icarus* **357**, 113690 (2020).
33. Rizk, B. et al. OCAMS: the OSIRIS-REx camera suite. *Space Science Reviews* **214**, 26 (2018).
34. DellaGiustina, D. et al. Properties of rubble-pile asteroid (101955) Bennu from OSIRIS-REx imaging and thermal analysis. *Nature Astronomy* **3**, 341–351 (2019).
35. Barnouin, O. et al. Digital terrain mapping by the OSIRIS-REx mission. *Planetary and Space Science* **180**, 104764 (2020).
36. Horz, F. & Cintala, M. Impact Experiments Related to the Evolution of Planetary Regoliths. *Meteoritics and Planetary Science Supplement* **31**, A65 (1996).
37. Flynn, G. J., Consolmagno, G. J., Brown, P. & Macke, R. J. Physical properties of the stone meteorites: Implications for the properties of their parent bodies. *Chemie der Erde* **78**, 269–298 (2018).
38. Macke, R. J., Consolmagno, G. J. & Britt, D. T. Density, porosity, and magnetic susceptibility of carbonaceous chondrites. *Meteoritics & Planetary Science* **46**, 1842–1862 (2011).
39. Sakatani, N., Ogawa, K., Arakawa, M. & Tanaka, S. Thermal conductivity of lunar regolith simulant JSC-1A under vacuum. *Icarus* **309**, 13–24 (2018).
40. Wada, K. et al. Asteroid Ryugu before the Hayabusa2 encounter. *Progress in Earth and Planetary Science* **5**, 82 (2018).
41. Ryan, A. J., Pino Muñoz, D., Bernacki, M. & Delbo, M. Full-Field Modeling of Heat Transfer in Asteroid Regolith: Radiative Thermal Conductivity of Polydisperse Particulates. *Journal of Geophysical Research: Planets* **125**, e2019JE006100 (2020).

42. Hanuš, J., Delbo, M., Ďurech, J. & Ali-Lagoa, V. Thermophysical modeling of main-belt asteroids from WISE thermal data. *Icarus* **309**, 297–337 (2018).
43. Burke, K. N. et al. Particle Size-Frequency Distributions of the OSIRIS-REx Candidate Sample Sites on Asteroid (101955) Bennu. *Remote Sensing* **13**, 1315 (2021).
44. Biele, J. et al. Macroporosity and Grain Density of Rubble Pile Asteroid (101955) Bennu. In *AGU Fall Meeting 2020* **1**, P037–04 (2020).
45. Gundlach, B. & Blum, J. A new method to determine the grain size of planetary regolith. *Icarus* **223**, 479–492 (2013).
46. DellaGiustina, D. N. et al. Variations in color and reflectance on the surface of asteroid (101955) Bennu. *Science* **370**, eabc3660 (2020).
47. Nakamura, T. et al. Itokawa dust particles: a direct link between S-type asteroids and ordinary chondrites. *Science* **333**, 1113–1116 (2011).
48. El Mir, C., Ramesh, K. T. & Delbo, M. The efficiency of thermal fatigue in regolith generation on small airless bodies. *Icarus* **333**, 356–370 (2019).
49. Hergenrother, C. W. et al. The operational environment and rotational acceleration of asteroid (101955) Bennu from OSIRIS-REx observations. *Nature Communications* **10**, 1291–10 (2019).
50. Watanabe, S. et al. Hayabusa2 arrives at the carbonaceous asteroid 162173 Ryugu—A spinning top-shaped rubble pile. *Science* **364**, 268–272 (2019).
51. Demura, H. et al. Pole and Global Shape of 25143 Itokawa. *Science* **312**, 1347–1349 (2006).
52. Christensen, P., Hamilton, V., Anwar, S., Mehall, G. & Lauretta, D. Origins, Spectral Interpretation, Resource Identification, Security, Regolith Explorer (OSIRIS-REx): OSIRIS-

REx Thermal Emission Spectrometer Bundle (2019). NASA Planetary Data System, urn:nasa:pds:orex.otes.

53. Rizk, B., Golish, D., DellaGiustina, D. & Lauretta, D. Origins, Spectral Interpretation, Resource Identification, Security, Regolith Explorer (OSIRIS-REx): OSIRIS-REx Camera Suite (OCAMS) Bundle (2019). NASA Planetary Data System, urn:nasa:pds:orex.ocams.
54. Deshapriya, J. D. P. OTES geoWriter. Zenodo, https://doi.org/10.5281/zenodo.4781752 (2021).
55. Ryan, A. Regolith heat transfer code for manuscript "Rock porosity drives regolith buildup on carbon-rich versus stony asteroids". Zenodo, http://doi.org/10.5281/zenodo.4763783 (2021).
56. Cambioni, S., Delbo, M. & Poggiali, G. Codes for two-component thermophysical analysis of asteroid (101955) Bennu. Zenodo, http://doi.org/10.5281/zenodo.4771035 (2021)

Acknowledgments

This material is based upon work supported by NASA under contract NNM10AA11C issued through the New Frontiers Program. We are grateful to the entire OSIRIS-REx team for making the encounter with Bennu possible, to C. Wolner and F. Murphy for editorial help, and to the OPAL infrastructure of the Observatoire de la Côte d'Azur (CRIMSON) for providing computational resources and support. S.C. thanks the University of Arizona for supporting this study. M.D., C.A., J.D.P.D and A.B. acknowledge the French space agency CNES. C.A. and M.D. acknowledge support from ANR "ORIGINS" (ANR-18-CE31-0014). C.A. was supported by the French National Research Agency under the project "Investissements d'Avenir" UCAJEDI ANR-15-IDEX-01. G.P. and J.R.B. were supported by Italian Space Agency grant

agreement INAF/ASI n. 2017-37-H.0. B.R. acknowledges financial support from the UK Science and Technology Facilities Council (STFC). E.A.C. thanks CSA, NSERC, CFI, MRIF and UWinnipeg for supporting this study.

Author Contribution

S.C. led the project, the interpretation of the results and manuscript development, and performed the thermophysical simulations and data analysis. M.D. provided the thermophysical software, performed the thermal cracking calculations and contributed to the interpretation of the results and to the development of the manuscript. G.P. developed the pipeline to retrieve OTES detailed survey data and performed rock mapping in PolyCam images. C.A. curated the discussion on meteoroid bombardment and contributed to the writing of the manuscript. A.J.R. contributed with the code to convert thermal inertia values in fine regolith particle size and developed the iterative approach to determine the cut-off value of thermal inertia together with S.C. J.D.P.D. contributed by extracting the observation geometry of the spacecraft and Bennu from mission kernels. R.-L.B. contributed by proposing important tests of the robustness of the results. E.A, W.F.B. and J.R.B. contributed to the interpretation of the data and the writing of the manuscript. D.N.D., K.N.B., C.A.B. and K.J.W. contributed by providing support in the interpretation of spacecraft imagery. J.P.E. and B.R. contributed to the data interpretation during the OSIRIS-REx Thermal Analysis Working Group meetings, and to design of the observations and data acquisition. M.A.B. and E.C. contributed to the interpretation of the results. D.S.L. made this study possible as the PI of the OSIRIS-REx mission and contributed to the discussion of the results.

Author information

Supplementary Information is available for this paper. Reprints and permissions information is available at www.nature.com/reprints. The authors declare no competing interests. Correspondence and requests for materials should be addressed to Saverio Cambioni (saveriocambioni@email.arizona.edu, saverio@caltech.edu).

Extended Data Fig. 1. The thermal inertia of Bennu's rocks and the surface abundance of fine regolith were measured in 122 quasi-randomly–distributed regions. a, OTES spots on Bennu plotted on the global basemap of Bennu[32] as function of longitude and latitude (red: 3:00 p.m. station, or EQ1; blue: 3:20 a.m. station, or EQ2). b, comparison between modelled and observed radiance for one of the 122 areas (ID: 609491396:610102222). c, comparison between the emissivity of Bennu and the residuals of the analysis for the spots 609491396:610102222; the residual curves closely resemble Bennu's emissivity, which is not modelled by our thermophysical model. The error bars correspond to 3 times the Noise Equivalent Spectral Radiance of the OTES instrument[15].

Extended Data Fig. 2. There is less fine regolith at the OSIRIS-REx's backup sampling site Osprey than at the primary sampling site Nightingale. Blue and yellow pixels represent areas where no particles bigger than 2 cm, ~ls, were mapped by ref. 43. The value $D_P \approx l_s$ is the upper limit for the sizes of fine regolith detected by our thermophysical model. There are less blue and yellow pixels at Osprey (image resolution: 0.3 cm pixel^{-1}, panels a, b) than at Nightingale (image resolution: 0.4 cm pixel^{-1}, panels c, d), implying that Osprey has less unresolved material than Nightingale. Consistently and independently, our thermophysical model indicates

615 $\alpha_{Osprey}<\alpha_{Nightingale}$ (Supplementary Table 1, spots 609505286:610098718 and
616 609504794:610100730, respectively).
617
618 **Extended Data Fig. 3. The fine regolith abundance derived from OTES data is lower than**
619 **the areas of unresolved material measured in Bennu's images.** Our visual mapping and size
620 measurement of rocks within two OTES spots: a, OTES spots 609493058:610103962; b, OTES
621 spots 609487186:610098206. In both areas, the values of α from our thermophysical solution are
622 smaller than the area of unresolved materials seen in the images. Given the coarse PolyCam[32]
623 resolution, it is possible that there are unmapped particles larger than l_s (but smaller than the
624 image resolution) that our thermophysical model detects as rocks and thus do not contribute to
625 the value of α.
626
627 **Extended Data Fig. 4. The correlation between Γ_R and α is statistically significant.** a,
628 Spearman correlation coefficient. b, Spearman p-value; a Spearman $p<0.05$ indicates that the
629 correlation between Γ_R and α is statistically significant. The figure corresponds to the results for
630 a value of regolith macroporosity of φ=40%.
631
632 **Extended Data Fig. 5. The correlation between Γ_R and α is robust against the choice of the**
633 **fine-regolith macroporosity.** The results for macroporosity φ=15% and φ=60% have Spearman
634 correlation coefficients 0.56±0.06 and 0.58±0.06, probability of non-correlation $p<0.05$, and are
635 within 3 standard deviations of the best-fit values for regolith macroporosity of φ=40% in 99%
636 and 92% of the cases, respectively. The correlations are robust against removing the areas whose
637 solutions are statistically distinct from the dataset with macroporosity φ=40% (Spearman

correlation index: 0.55±0.07 and $p<0.05$ in 100% of 10,000 trials). The error bars correspond to 1 standard deviation (Supplementary Table 1; Methods) computed on ~450 and ~880 samples on average. The results for a regolith macroporosity of φ=40% are described in the main text (Figure 1).

Extended Data Fig. 6. The correlation between Γ_R and α is not an artefact of thermophysical modelling. We fit model radiances emitted by a single triangular facet with zero roughness; if the thermal inertia $\Gamma \leq \Gamma_c = 100$ $Jm^{-2}K^{-1}s^{-0.5}$, then α=100%, and if $\Gamma_c<\Gamma<2{,}500$ $Jm^{-2}K^{-1}s^{-0.5}$, then α = 0%. We retrieve the expected step function of α as a function of Γ, indicating that the correlation in Figure 1 is unlikely to be an artefact of the model. The error bars correspond to 1 standard deviation computed on ~ 1.76×10^4 samples on average (Methods).

Extended Data Fig. 7. The correlation between Γ_R and α is not a geometric effect due to boulders' sizes. a, PolyCam image of the surface corresponding to spots 609486110:610097198 where α is low probably because the spots are filled by a large, dark boulder. b, PolyCam image of the surface corresponding to spots 609495164:610106090 where α does not correlate with the size of the largest boulder; this is representative of most of the surveyed areas. c, plot of α as function of the percentage of the OTES spot covered by the largest boulder on the surface. The Spearman test reveals that these two quantities have a probability of non-correlation above the critical threshold of 0.05 in 99.99% of 10,000 trials. This indicates that the Γ_R-α correlation of Figure 1 is not the result of geometric effects. The error bars in panel c correspond to 1 standard deviation (Supplementary Table 1; Methods) computed on ~ 670 samples on average.

Extended Data Fig. 8. The time required to thermally break rocks is shorter for low-porosity rocks than for high-porosity rocks. We consider the asteroid to be in near-Earth space and explore a range of rotation periods corresponding to the shaded areas. The latter is to take into account changes in the current rotation periods (4.296 h and 12.1 h for Bennu and Itokawa, respectively) that these asteroids may have experienced in the past[49] due to the Yarkovsky–O'Keefe–Radzievskii–Paddack (YORP) effect. We estimate that in their main belt source region, at about 2.3 au from the Sun, the time to break is ~60 times longer.

Extended Data Fig. 9. Examples of in-situ boulder fragmentation on Bennu. a, a 5.4 m-diameter boulder located at 22° N 157° E. b, a 5.6 m-diameter boulder located at 42° N 170° E. c, a 5.3 m-diameter boulder located at 57° N 304° E. d, a 5 m-diameter boulder located at 39° S 203° E. The images are from the global mosaic[32] acquired by the PolyCam[33] imager of OCAMS.

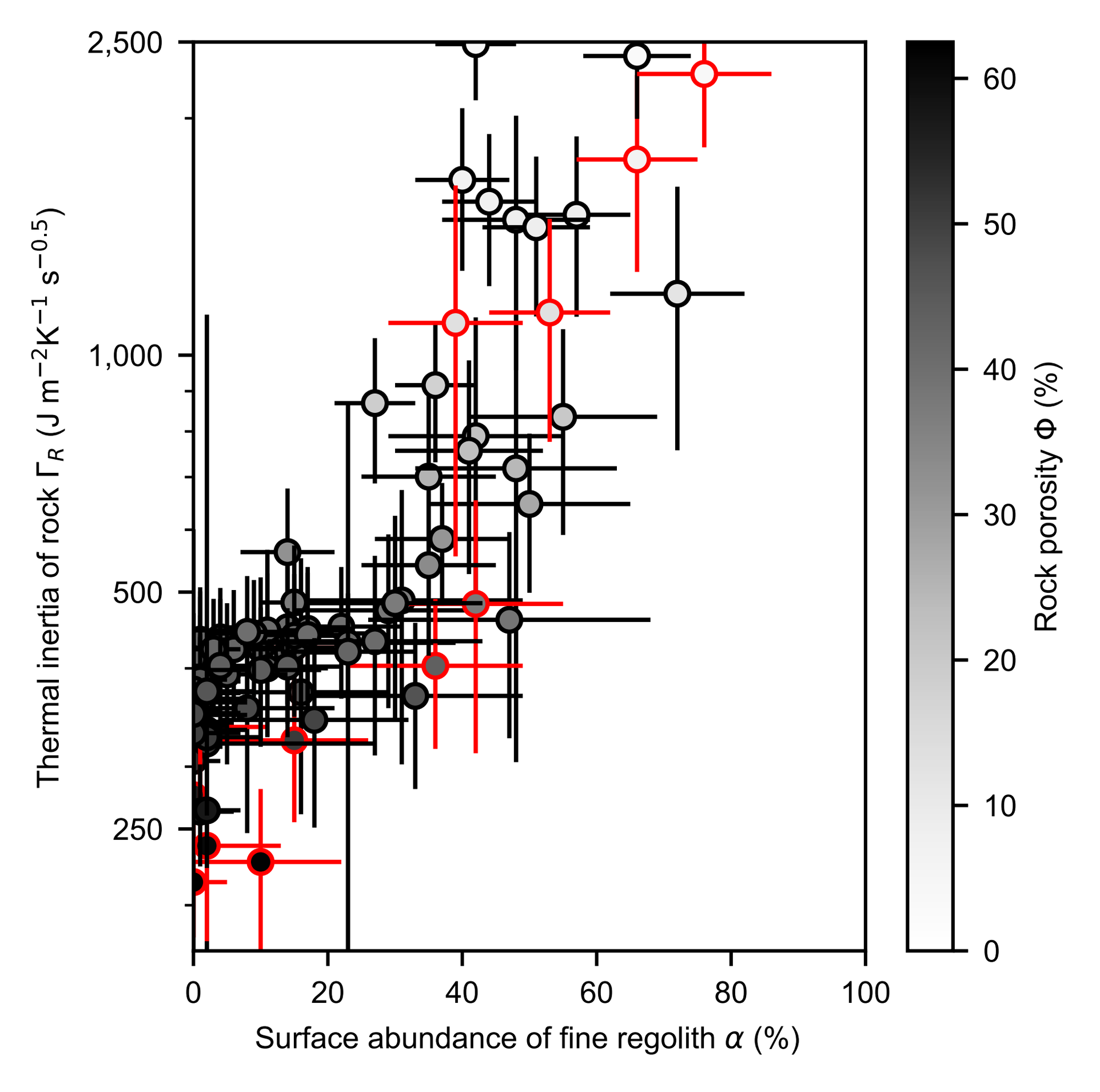
2,500
1,000
500
250
Thermal inertia of rock Γ_R (J m^{-2}K^{-1} s$^{-0.5}$)
0
20
40
60
80
100
Surface abundance of fine regolith α (%)
60
50
40
30
20
10
0
Rock porosity Φ (%)

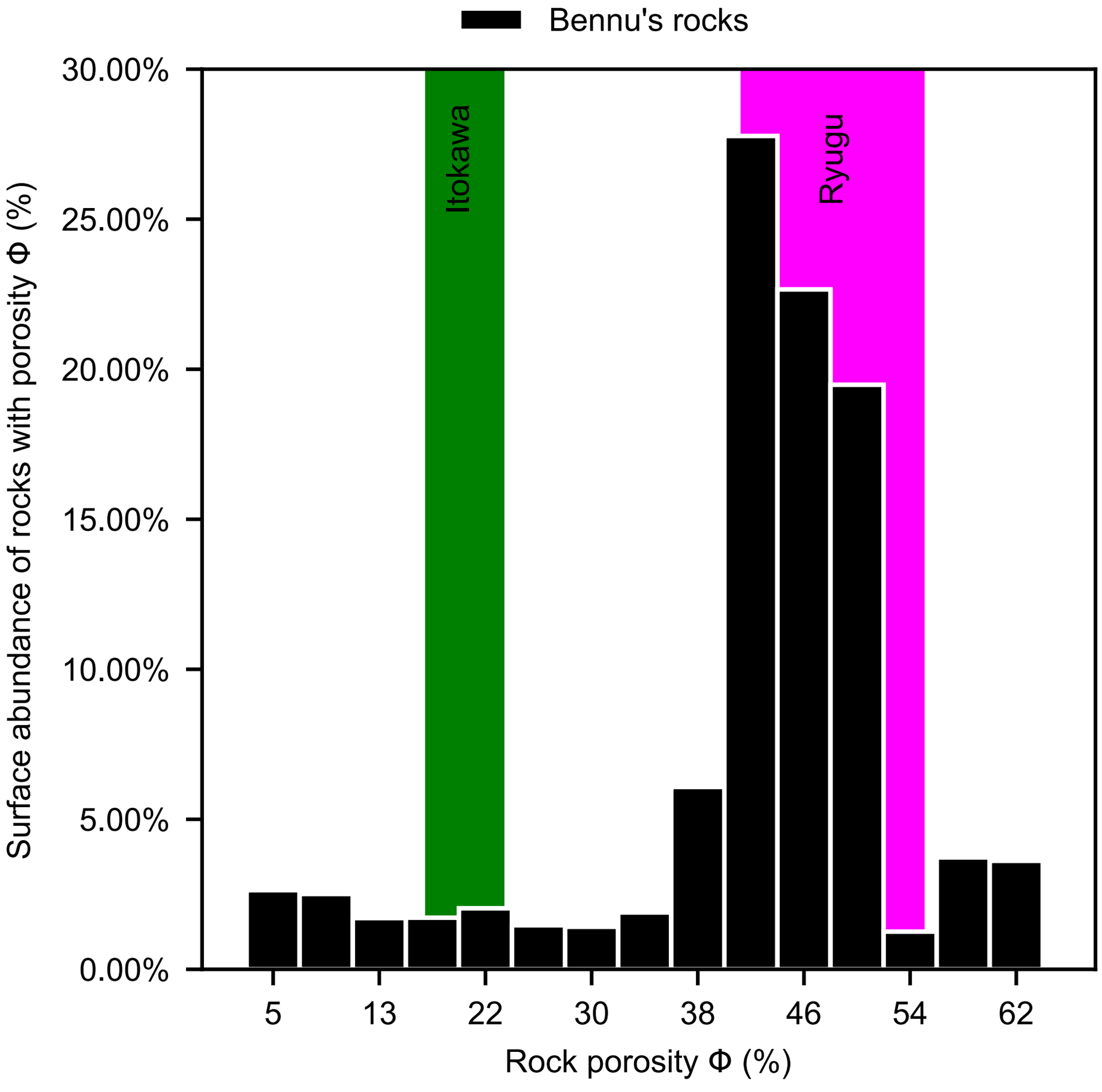
Bennu's rocks
Itokawa
Ryugu
30.00%
25.00%
20.00%
15.00%
10.00%
5.00%
0.00%
Surface abundance of rocks with porosity Φ (%)
5
13
22
30
38
46
54
62
Rock porosity Φ (%)

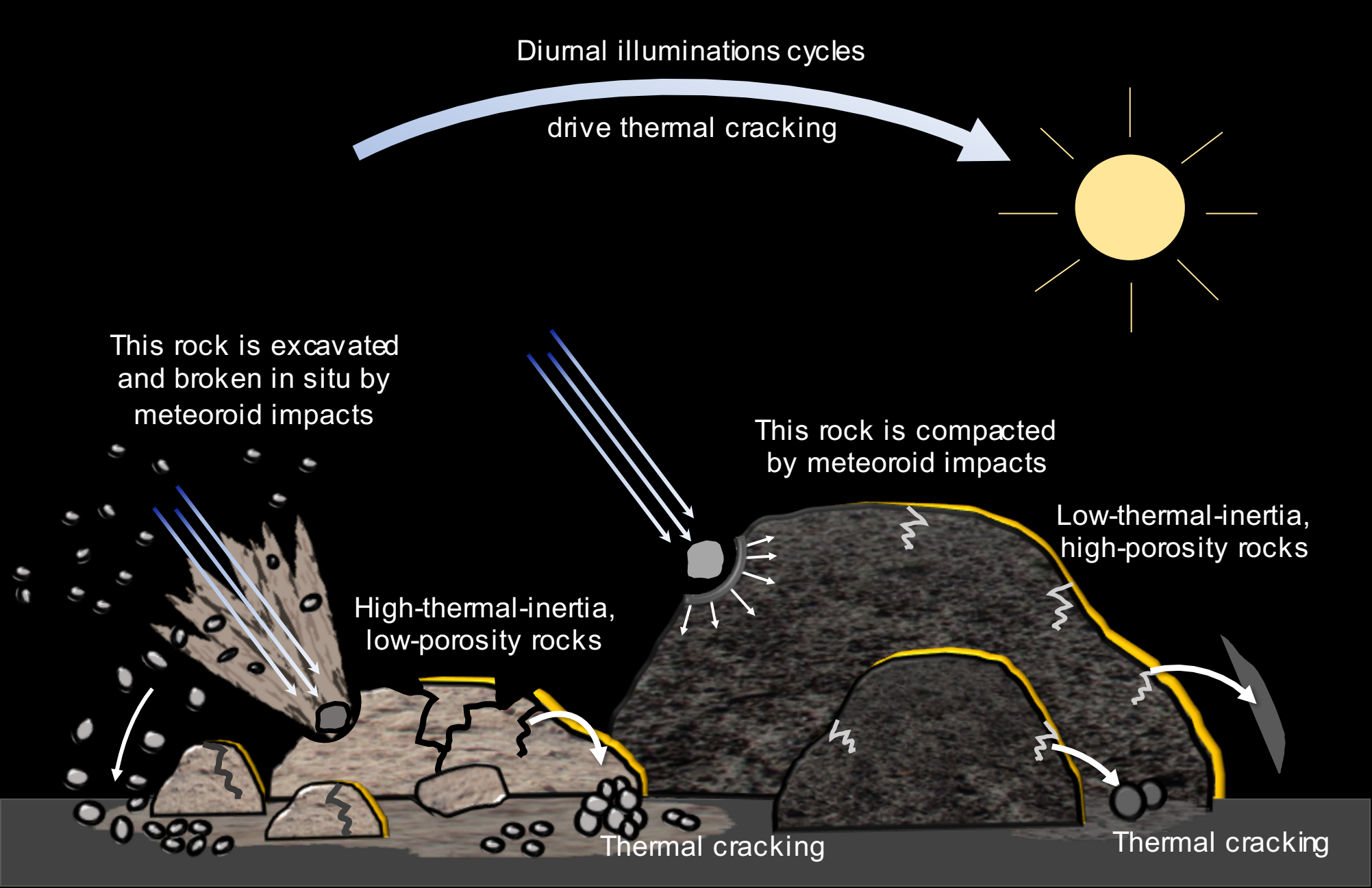
Diurnal illuminations cycles
drive thermal cracking
This rock is excavated and broken in situ by meteoroid impacts
This rock is compacted by meteoroid impacts
Low-thermal-inertia, high-porosity rocks
High-thermal-inertia, low-porosity rocks
Thermal cracking
Thermal cracking

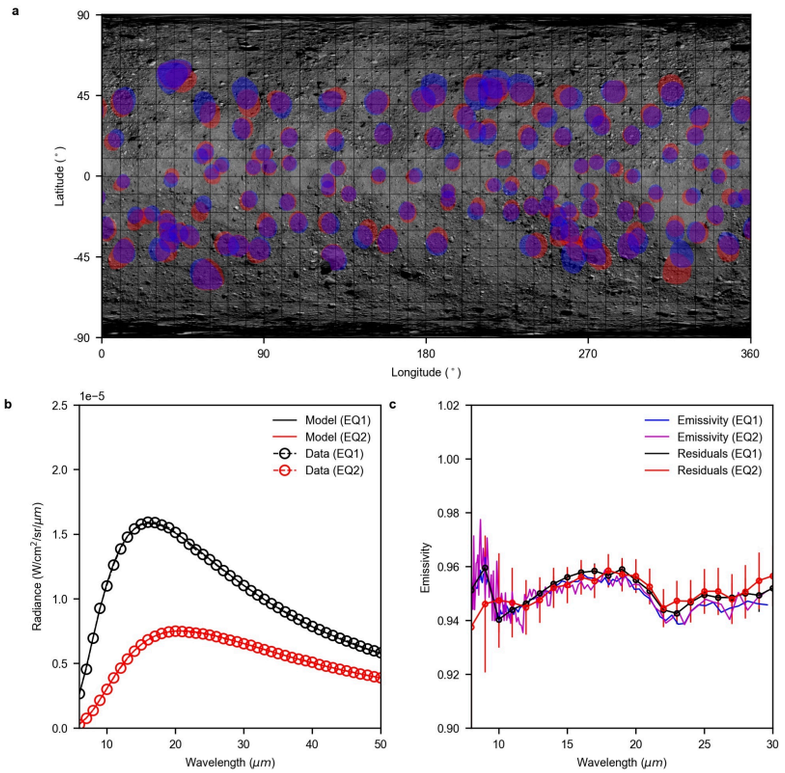
a
90
45
0
-45
-90
Latitude (°)
0
90
180
270
360
Longitude (°)
b
1e−5
2.5
2.0
1.5
1.0
0.5
0.0
Radiance (W/cm²/sr/μm)
10
20
30
40
50
Wavelength (μm)
Model (EQ1)
Model (EQ2)
Data (EQ1)
Data (EQ2)
c
1.02
1.00
0.98
0.96
0.94
0.92
0.90
Emissivity
10
15
20
25
30
Wavelength (μm)
Emissivity (EQ1)
Emissivity (EQ2)
Residuals (EQ1)
Residuals (EQ2)

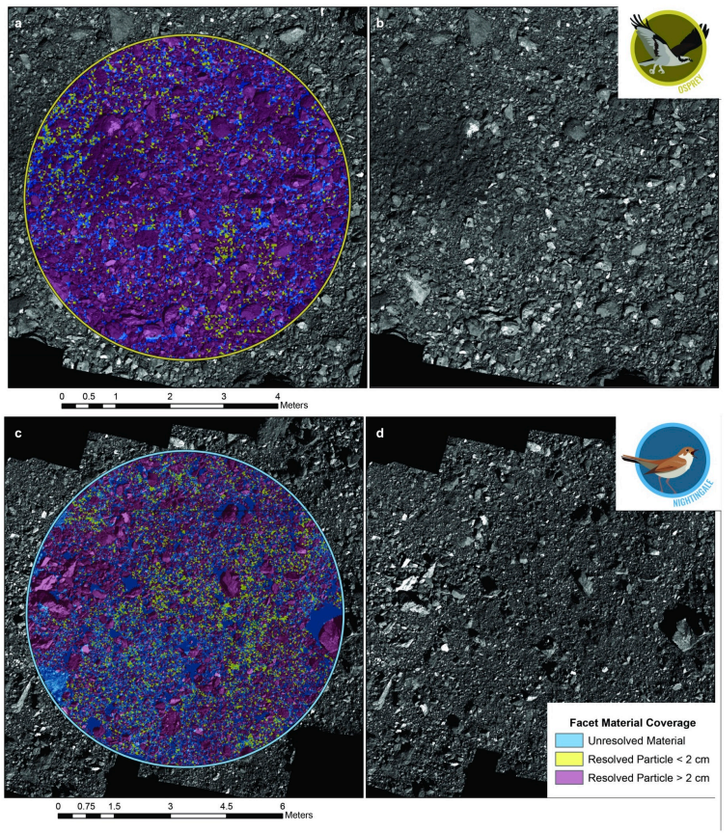
a
b
OSPREY
0 0.5 1 2 3 4
Meters
c
d
NIGHTINGALE
Facet Material Coverage
Unresolved Material
Resolved Particle < 2 cm
Resolved Particle > 2 cm
0 0.75 1.5 3 4.5 6
Meters

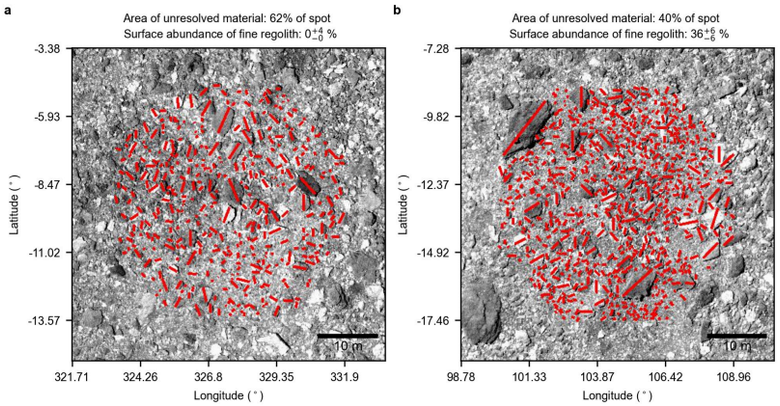
a
Area of unresolved material: 62% of spot
Surface abundance of fine regolith: 0^{+4}_{-0} %
-3.38
-5.93
-8.47
-11.02
-13.57
Latitude (°)
10 m
321.71
324.26
326.8
329.35
331.9
Longitude (°)
b
Area of unresolved material: 40% of spot
Surface abundance of fine regolith: 36^{+6}_{-6} %
-7.28
-9.82
-12.37
-14.92
-17.46
Latitude (°)
10 m
98.78
101.33
103.87
106.42
108.96
Longitude (°)

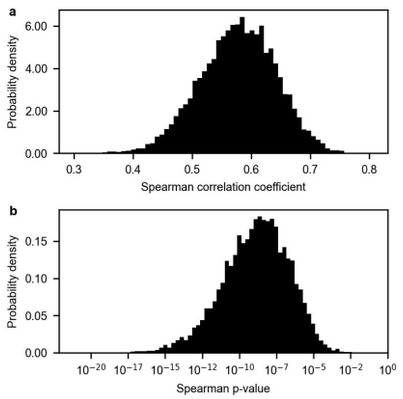
a
Probability density
6.00
4.00
2.00
0.00
0.3
0.4
0.5
0.6
0.7
0.8
Spearman correlation coefficient
b
Probability density
0.15
0.10
0.05
0.00
10^{-20} 10^{-17} 10^{-15} 10^{-12} 10^{-10} 10^{-7} 10^{-5} 10^{-2} 10^{0}
Spearman p-value

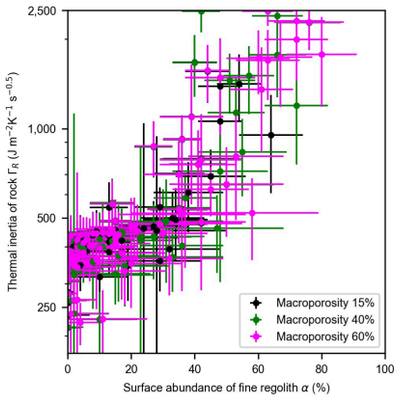
2,500
1,000
500
250
0
20
40
60
80
100
Thermal inertia of rock Γ_R (J m^{-2}K^{-1} s$^{-0.5}$)
Surface abundance of fine regolith α (%)
Macroporosity 15%
Macroporosity 40%
Macroporosity 60%

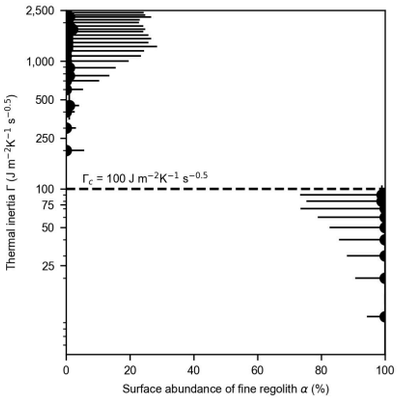
2,500
1,000
500
250
100
75
50
25
Thermal inertia Γ (J m^{-2}K^{-1} s$^{-0.5}$)
Γ_c = 100 J m^{-2}K^{-1} s$^{-0.5}$
0
20
40
60
80
100
Surface abundance of fine regolith α (%)

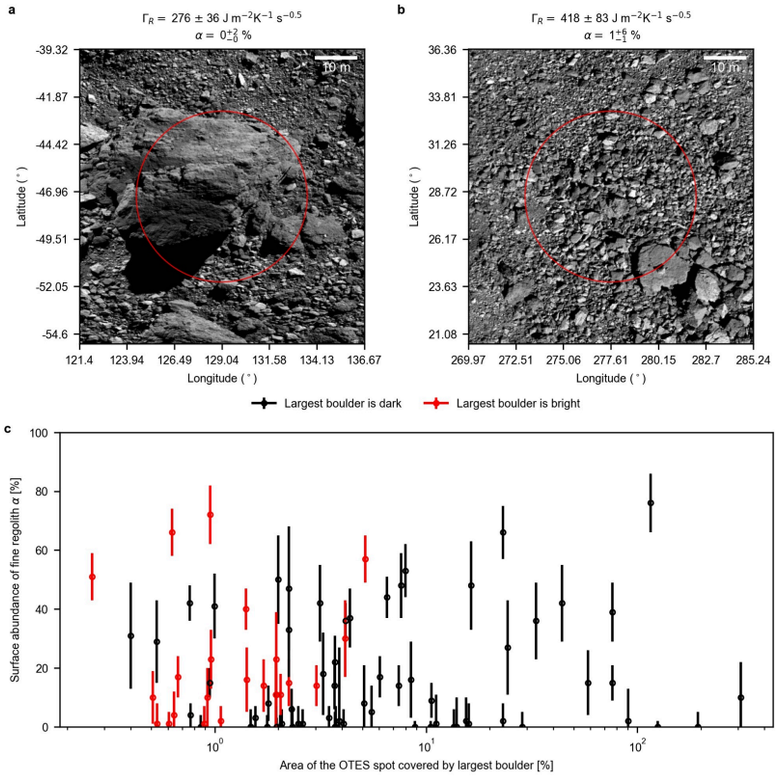
a
$\Gamma_R = 276 \pm 36$ J m^{-2}K^{-1} s$^{-0.5}$
$\alpha = 0^{+2}_{-0}$ %
19 m
-39.32
-41.87
-44.42
-46.96
-49.51
-52.05
-54.6
Latitude (°)
121.4
123.94
126.49
129.04
131.58
134.13
136.67
Longitude (°)
b
$\Gamma_R = 418 \pm 83$ J m^{-2}K^{-1} s$^{-0.5}$
$\alpha = 1^{+6}_{-1}$ %
10 m
36.36
33.81
31.26
28.72
26.17
23.63
21.08
Latitude (°)
269.97
272.51
275.06
277.61
280.15
282.7
285.24
Longitude (°)
Largest boulder is dark
Largest boulder is bright
c
Surface abundance of fine regolith α [%]
100
80
60
40
20
0
10^0
10^1
10^2
Area of the OTES spot covered by largest boulder [%]

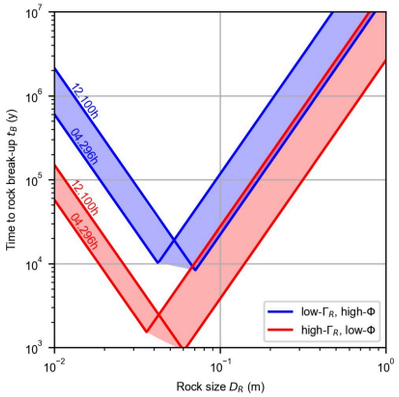
Time to rock break-up t_S (y)
Rock size D_R (m)
12.100h
04.296h
12.100h
04.296h
low-Γ_R, high-Φ
high-Γ_R, low-Φ

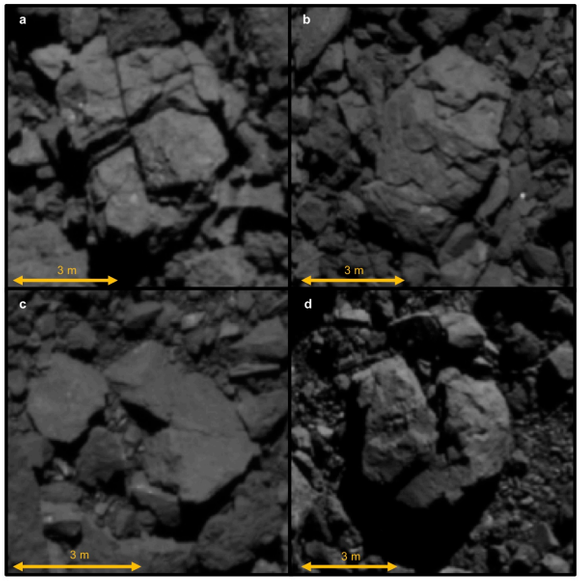
a
3 m
b
3 m
c
3 m
d
3 m